HHS Public Access

Author manuscript

Biomaterials. Author manuscript; available in PMC 2018 July 01.

Published in final edited form as:

Biomaterials. 2017 July ; 133: 119–131. doi:10.1016/j.biomaterials.2017.03.042.

Distinct ON/OFF fluorescence signals from dual-responsive activatable nanoprobes allows detection of inflammation with improved contrast

Mathieu L. Viger, Dr.[1], **Guillaume Collet, Dr.**[1], **Jacques Lux**[2], **Viet Anh Nguyen Huu**[3], **Monica Guma**[4], **Alexandra Foucault-Collet, Dr.**[1], **Jason Olejniczak**[5], **Shivanjali Joshi-Barr, Dr.**, **Gary S. Firestein**[4], and **Adah Almutairi, Prof.**[1,6]

[1]Skaggs School of Pharmacy and Pharmaceutical Sciences, KACST - UCSD Center for Excellence in Nanomedicine and Engineering, University of California, San Diego, 9500 Gilman Dr., La Jolla, California 92093-0600, USA

[2]UT Southwestern Medical Center, Department of Radiology, 5323 Harry Hines Blvd., Dallas, Texas 75390-8896, USA

[3]Department of Nanoengineering, University of California, San Diego, 9500 Gilman Dr., La Jolla, California 92093-0448, USA

[4]Division of Rheumatology, Allergy and Immunology, School of Medicine, University of California, San Diego, 9500 Gilman Drive, La Jolla, California 92093-0656, USA

[5]Department of Chemistry and Biochemistry, University of California, San Diego, 9500 Gilman Drive, La Jolla, California 92093-0332, USA

[6]Skaggs School of Pharmacy and Pharmaceutical Sciences, KACST - UCSD Center for Excellence in Nanomedicine and Engineering, University of California, San Diego, 9500 Gilman Dr., La Jolla, California 92093-0600, USA

Abstract

Visualization of biochemical changes associated with disease is of great clinical significance, as it should allow earlier, more accurate diagnosis than structural imaging, facilitating timely clinical intervention. Herein, we report combining stimuli-responsive polymers and near-infrared fluorescent dyes (emission max: 790 nm) to create robust activatable fluorescent nanoprobes capable of simultaneously detecting acidosis and oxidative stress associated with inflammatory microenvironments. The spectrally-resolved mechanism of fluorescence activation allows removal of unwanted background signal (up to 20-fold reduction) and isolation of a pure activated signal, which enables sensitive and unambiguous localization of inflamed areas; target-to-background ratios reach 22 as early as 3 h post-injection. This new detection platform could have significant

Correspondence to: Adah Almutairi.

Supporting Information: Supplementary data associated with this article can be found, in the online version, at…

clinical impact in early detection of pathologies, individual tailoring of drug therapy, and image-guided tumor resection.

Graphical abstract

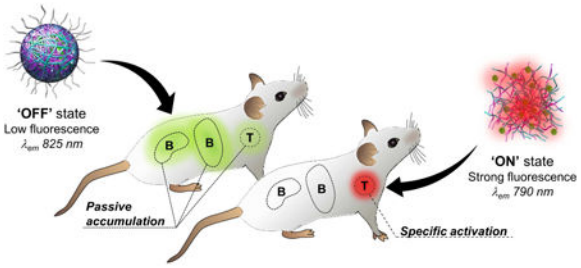

Keywords

Molecular imaging; inflammatory microenvironments; NIR optical nanoprobes; stimuli-responsive polymers; spectrally-resolved imaging

1. Introduction

Visualizing molecular features of pathological tissue micro-environments rather than the structural consequences of these abnormalities has the potential to facilitate detection of lesions at a time when treatment is most effective [1, 2]. For example, detecting cancer at an early stage is one of the most important strategies to reduce morbidity and mortality [3]. Near-infrared (NIR) optical imaging, being non-invasive, safe, highly sensitive and able to provide real-time image guidance, is emerging as a promising tool to help meet this need [4]. It is admitted that the diagnostic performance (i.e., sensitivity, accuracy and limit of detection) of a molecular imaging platform depends on its capacity to provide high specific signal relative to background signal originating from normal tissues (target-to-background ratios, T/B) [5]. Recently, nanomaterial-based optical probes have been developed to enhance detection sensitivity and extend the period available for imaging as they carry a large number of reporters, offer high surface to volume ratio causing higher binding capacity and are cleared from circulation slowly because of their larger size [6, 7]. Although this strategy improves physical detection (i.e., signal strength), achieving sufficient specificity remains a significant challenge because of the predominance of accumulation in liver and other blood-filtering organs (e.g., kidneys, and spleen) which can generate background signal, obscure weaker details, cause false positives, and decrease confidence in true positives [8]. A number of approaches (e.g., reconstruction algorithms, image subtraction) have been designed to mitigate the detrimental effect of background signal [9, 10]. While some of these methodologies work well for autofluorescence removal, they are not ideal when the noise originates from nonspecific accumulation of imaging agents.

Optical molecular probes designed to be activatable, that is, silent (‘OFF’ state) until they interact with the biological target and turn ‘ON’, can provide a decrease in background signal, hence superior accuracy and limits of detection [11-14]. However, the nature of the activatable signal underlying optical probes can have a tremendous influence on their

performance in vivo. For instance, in most intensity-based approaches, the inevitable residual 'OFF' state signal, which shares the same emission signature as the 'ON' state signal, can be picked up by the detector and contribute to increasing the noise level, later decreasing the detection threshold [15-18]. Due to the limited amount of biomarkers and the predominance of nonspecific accumulation, the seemingly low basal signal of the 'OFF' state can become substantial compared to the specific signal originating from the activated probes. This is especially problematic shortly after injection when the level of activation is not yet high enough to yield good contrast. On the other hand, spectrally-resolved detection systems [19-22], characterized by emission peak shifts, offer improved contrast and detection accuracy due to lower crosstalk and easier discrimination between target and non-specific background signals [23, 24]. Owing to the ability to perform ratiometric measurements, spectral-based probes can also provide quantitative information [25, 26].

Herein, we developed a novel class of activatable nanoprobes (NPs, Figure 1), leveraging on the advantages of nanomaterial-based and spectrally-resolved detection schemes, which enabled fluorescence detection of inflamed areas with large T/B reaching as high as 22, only 3 h post-injection. In this strategy, stimuli-responsive dextran-based materials (Figure S1, see Experimental Section, *Materials*) [27, 28], whose water solubility changes upon exposure to biomarkers of inflammation (i.e., acidosis and oxidative stress) [29, 30], are used to effectively control the fluorescent intensity and the spectral profile of multiple NIR-emitting IR-780 dye molecules at once (Figure 1). To maximize the signal strength, we rely on a 'dual responsivity' approach to build NPs capable of simultaneous synergistic response to acidic pH and elevated levels of hydrogen peroxide (H_2O_2), two biomarkers intrinsically associated with inflammation processes [31, 32]. Upon intravenous injection, the nanoprobes circulate in the blood stream and through healthy tissues where they remain in their 'OFF' state (Figure 1B, healthy tissue). In pathological microenvironments, the incidence of vessel leakiness and compromised blood flow results in transvascular transport of NPs into the inflamed tissues and/or retention in blood capillaries where they are selectively turned 'ON' by the acidic and oxidative environments (Figure 1B, pathological tissue) [33-35]. To minimize the contribution of nonspecific accumulation, we take advantage of the distinct emission signatures of the NPs' states (silenced vs. activated) to spectrally resolve the detected signal and isolate exclusively the activated signal in inflamed areas.

2. Materials and Methods

Materials

Dextran (9-11 kDa), poly(lactic-co-glycolic acid) (PLGA, ratio: 50:50; Mw: 7-17 kDa; alkyl ester terminated), IR-780 iodide (98%), indocyanine green (ICG, USP reference standard), 2-methoxypropene (97%), pyridinium *p*-toluenesulfonate (99%), 4-(Hydroxymethyl)phenylboronic acid pinacol ester (97%), sodium sulfate (99%), 4-(dimethylamino)pyridine (DMAP), carbonyldiimidazole (≥97%), magnesium sulfate (≥99.5%), and triethylamine (≥99%), were purchased from Sigma Aldrich. Pluronic® F-127 (poloxamer 407, 13 kDa) was purchased from O-BASF. Ovalbumin Alexa Fluor® 594 conjugate (OVA-AF594) and bovine serum albumin fluorescein conjugate (BSA-FITC) were

purchased from Life Technologies. Fetal bovine serum (FBS) was purchased from Omega Scientific. Chloroform ($CHCl_3$, 99.8%, EMD), acetone (Fisher Scientific), dimethyl sulfoxide (DMSO, 99%, Aldrich), tetrahydrofuran (THF, Aldrich), ethyl acetate (EtOAc, Fisher Scientific), dichloromethane (DCM, Fisher Scientific) and Dulbecco's Phosphate-Buffered Saline (DPBS, 1×, Life Technologies) were used without further purification. De-ionized water (DI H_2O) was purified from a Millipore system (18.2 MΩ).

Responsive modified dextrans—Dextran responsive to acidic pH is obtained in a one-step process by protecting the alcohols on the dextran backbone with acid-labile acetal groups (Figure S1A, left).[28] Briefly, 2-methoxypropene (3.4 mL, 37 mmol) and pyridinium *p*-toluenesulfonate (15.6 mg, 62 μmol) were added to a solution of dextran (1 g, 100 μmol) in anhydrous DMSO (10 mL) at room temperature and the reaction mixture was quenched with triethylamine after 20 min. In our study, acetalated dextran presented a relative cyclic acetal content of 38% (Figure S1B). Details on determination of cyclic:acylic acetal ratio can also be found in the aforementioned publication. The oxidation-sensitive dextran was obtained according to procedures previously published by Broaders *et al.*[27] In brief, carbonyldiimidazole (5.8 g, 36 mmol) was added to a solution of 4-(hydroxymethyl)phenylboronic acid pinacol ester (6.11 g, 18 mmol) in DCM (24 mL) and stirred for 1 h. The resulting carbonyldiimidazole-activated boronic ester carbamate was worked up according to the procedure found in Broaders *et al.*[27] The carbonyldiimidazole-activated boronic ester carbamate (46 mg, 140 μmol, 2.0 eq), along with DMAP (19.4 mg, 158 μmol), was added to a solution of dextran (22.5 mg, 2.25 μmol) in anhydrous DMSO (0.4 mL) and shaken overnight at 37 °C to yield the oxidation-sensitive dextran. In the final product, 30% of the anhydroglucose units were modified (Figure S1C). Details on determination of arylboronic ester modification can also be found in Broaders *et al.*[27]

Preparation and characterization of the polymeric nanoprobes

Responsive polymer(s) (10 mg) was dissolved in DMSO (0.075 mL) and diluted with a solution containing both IR-780 (1 mg) and poloxamer 407 (1 mg) in $CHCl_3$ (0.20 mL). The prepared solutions were electrosprayed at 28 kV (Gamma High Voltage, ES30) at a flow rate of 0.1 mL/h (KD Scientific) using a 25 gauge blunted needle. Samples were collected onto microscope glass slides on an aluminum plate collector at a distance of 30 cm. The particles were removed from their glass slide substrate by sonication and collected by centrifugation (20,000 RPM, 20 min).

The size and morphology of the nanoprobes (NPs) were examined by SEM (Agilent, 8500) and TEM (FEI, Tecnai G2 Spirit). The hydrodynamic diameter and particles count rate were obtained by DLS (Malvern, Zetasizer). Particle diameter distributions were extracted from recorded dark-field images and SEM photographs using NIS Elements (Nikon) and ImageJ software (NIH). The amount of dye incorporated into the various NPs was determined by absorption spectroscopy using a dual beam UV–Vis–NIR Spectrophotometer (UV-3600, Shimadzu). To do so, IR-780-loaded NPs (1 mg) were completely solubilized in $CHCl_3$ (50 mL) followed by absorption measurements and quantification of the dye concentration by linear calibration.

Quantification of protein adsorption

Aliquots of nanoprobes (0.1 mg) were incubated overnight with BSA-FITC (0.1 mg) and OVA-AF594 (0.1 mg) in 1 mL of PBS 1×. After incubation, the samples were collected and washed by centrifugation (20,000 RPM, 20 min) to remove any unbound proteins and dispersed in 1 mL of PBS 1×. The fluorescence of the nanoprobes was measured and the protein concentration quantified by linear calibration. The surface density coverage in ng/cm^2 was obtained by dividing the amount of bound protein to the total surface area of the nanoprobes.

In vitro serum stability

Aliquots of nanoprobes (0.1 mg) were diluted in 1 ml of FBS. The mixtures were incubated at 37 °C. At each designated time point (t = 0, 1, 2, 4, 6, 8, 24 h), samples were collected and washed by centrifugation (20,000 RPM, 20 min) to remove the serum and dispersed in 1 mL of PBS 1×, followed by acquisition of DLS-based count rates and fluorescence spectra.

In vitro measurement of fluorescence activation

Fluorescence emission spectra of the NPs (λ_{ex} = 720 nm, λ_{em} = 750-900 nm) were obtained using a Fluorolog spectrofluorometer (Horiba Jobin-Yvon), whereas kinetics of fluorescence activation (λ_{ex} = 745 nm, λ_{em} 800 nm) were acquired using a fluorescence plate reader (FlexStation® 3, Molecular Devices). Fluorescence images of the NPs were captured on an in vivo imaging system (IVIS® Spectrum) using a selection of IR-780-specific filters (Filter set 1: λ_{ex} = 745 nm, λ_{em} = 790-810 nm; Filter set 2: λ_{ex} = 745 nm, λ_{em} = 810-830 nm; Filter set 3: λ_{ex} = 745 nm, λ_{em} = 830-850 nm). A two-component spectral unmixing sequence was carried out using the built-in algorithm of Living Image 4.3.1 software to separate the ‘OFF’ state signal (unactivated NPs) and the ‘ON’ state signal (activated NPs). We used ‘automatic mode’ spectral unmixing, which compares intensity changes throughout the field of view that result from the filter scan against the spectral profile of the two emission states (‘OFF’ and ‘ON’ state). The unmixed spectral images appear as two-component images (one for each state) and a composite image color-coded for the two emission states (green for ‘OFF’ and red for ‘ON’). The ‘component images’ are measured with ROIs for quantification, while the ‘composite image’ allows a clear presentation of the fluorescent foci.

pH activation—NPs (0.2 mg/mL) were dispersed in phosphate-buffered saline (PBS) pH 7.4. Aliquots of NPs (0.25 mL, 0.05 mg) were centrifuged (20,000 RPM, 20 min) and diluted with either PBS (pH 7.4, pH 7.0) or citrate buffer (pH 6.0) to a final concentration of 0.1 mg/mL (0.5 mL).

H_2O_2 activation—NPs (0.2 mg/mL) were dispersed in PBS pH 7.4. Aliquots of NPs (0.25 mL, 0.05 mg) were centrifuged (20 000 RPM, 20 min) and diluted with PBS (pH 7.4) solutions containing different concentration of H_2O_2 (0, 0.1, 0.25, 0.5, 0.75, 1 mM) to a final concentration of 0.1 mg/mL (0.5 mL).

H_2O_2 activation at different pH—NPs (0.2 mg/mL) were dispersed in PBS pH 7.4. Aliquots of NPs (0.25 mL, 0.05 mg) were centrifuged and diluted with either PBS (pH 7.4,

pH 7.0) or citrate buffer (pH 6.0) solutions containing different concentration of H_2O_2 (0, 0.1, 0.25, 0.5, 0.75, 1 mM) to a final concentration of 0.1 mg/mL (0.5 mL). All experiments were run in triplicate. The sensitivity was obtained by determining the slope of the linear portion of the data plot (from 0 to 0.25 mM).

Animal models and in vivo/ex vivo NIR fluorescence imaging

All animal experiments were performed in agreement with the Institutional Animal Care and Use Committee (IACUC).

Mouse 4T1 breast tumor model—Tumor growth was induced by grafting 4T1 cells (1×10^6 cells/mouse) subcutaneously on the right shoulder of BALB/c mice (4-6 weeks, Harlan Sprague Dawley). Ten days after the graft, tumor sizes reached approximatively 170 mm^3. The NPs (non-responsive, pH-responsive, H_2O_2-responsive, dual-responsive; 1 mg/mL in PBS) and free dye controls (IR-780, ICG; 0.1 mg/mL in PBS) were administered (0.1 mL) 10 days post-tumor implantation through retro-orbital injections (n_{tot} = 30, n = 5 for each group). The injected amount of free dye is equal to the total theoretical amount of dye encapsulated in the responsive polymer particles.

K/BxN serum-transfer model of arthritis—Arthritis was induced in C57BL/6 mice (6-8 weeks, Harlan Sprague Dawley) by the intraperitoneal administration of 150 μL of serum from K/BxN transgenic mice. Arthritis scores were assessed using a semi-quantitative clinical scoring system. The joint-specific inflammatory responses were maximal 5 days post-serum injections. The NPs (non-responsive, pH-responsive, H_2O_2-responsive, dual-responsive; 1 mg/mL) were administered (0.1 mL) 5 days post-serum transfer through retro-orbital injections (n_{tot} = 16, n = 4 for each group).

Carrageenan-induced paw inflammation—Acute swelling/inflammation of the left hind paw (BALB/c mice, 4-6 weeks, Harlan Sprague Dawley) was induced by injecting carrageenan solution (25 μL, 2% w/v in PBS) into the sub-plantar region. The inflammatory response (i.e., increase in paw volume) was maximal 2-3 h post-carrageenan injection. The NPs (non-responsive, pH-responsive, H_2O_2-responsive, dual-responsive; 1 mg/mL in PBS) were administered (0.1 mL) two hours post-carrageenan injection through retro-orbital injections (n_{tot} = 20, n = 5 for each group). Dual-responsive nanoprobes were also injected in healthy mice (n = 5) and studied by fluorescence imaging.

In vivo spectral fluorescence images were captured by the IVIS® Spectrum pre- and post-injection of NPs (0, 1, 2, 3, 5, 7 h for all models; + 24, 36, 48, 60, 72, 84, 96 h for breast tumor model). All injections and imaging acquisitions were performed under anesthesia (2% isoflurane in O_2, 1 L/min) on hairless mice. Hair was removed using shaving and depilatory cream (i.e., Nair®) 24 h before injecting the NPs. At each time point, the mice were scanned with an acquisition sequence comprised of background- and dye-specific filter selections. For tissue autofluorescence, mice were irradiated with a 465 ± 30 nm light and the emission was collected from 520 to 580 nm (bandwidth: 20 nm), whereas for IR-780/ICG, the mice were irradiated at 745 ± 15 nm and the emission was collected from 800 to 840 nm (bandwidth: 20 nm). The following settings were used to obtain the fluorescence images:

exposure time = 1 and 3 s, binning value = 8, Fstop value = 2, field of view = 22 cm. Regions of interest (ROI) were drawn over the major background contributors (e.g. liver, spleen, kidneys, bowel) and inflamed areas (tumors, arthritic joints and inflamed hind paws), and the average radiance (p/s/cm^2/sr) was extracted for each ROI. The whole body signal clearance was quantified by adjusting the ROI to cover the entire mouse. For each acquired sequence, a two-component spectral unmixing sequence was carried out using the built-in algorithm of Living Image 4.3.1 software to separate the 'OFF' state signal (unactivated NPs) and the 'ON' state signal (activated NPs), as well as the tissue autofluorescence.

After imaging, the mice were euthanized and the inflamed tissues and major organs were excised. Each organ was rinsed with PBS and placed into a Petri dish prior to imaging using the IVIS® Spectrum. The same acquisition and unmixing sequences were used to image the organs ex vivo. For fluorescence signal quantification, a ROI was drawn over each individual organ and adjusted to its shape, and the average radiance (p/s/cm^2/sr) was extracted. Inflamed areas (i.e., tumors, inflamed joints, and inflamed paws)-to-background signal ratios were obtained by dividing the mean average radiance calculated for the inflamed regions to that of the background. All in vivo data are presented as the mean ± standard error of the mean (s.e.m.).

Serum collection and analysis

At designated times (t = 3, 24 and 96 h) after injection of either dual-NPs (0.1 mg) or 1× PBS (pH 7.4) to 4T1 breast carcinoma bearing mice (n_{tot} = 8, n = 4 per group), blood samples were obtained under anesthesia (2% isoflurane in O_2, 1 L/min) by cheek bleed induced with a submandibular lancet. Blood was collected by dripping into collection tubes containing serum separator additive (BD Microtainer®). Blood samples were allowed a minimum of 30 min at room temperature for a clot to stabilize. The samples were then centrifuged (2 min, 8000 rpm) and the serum portions (supernatant) were isolated and stored at -80°C. Serum biochemistry, which included albumin (ALB), alkaline phosphatase (ALP), alanine aminotransferase (ALT), amylase (AMY), blood urea nitrogen (BUN), calcium (CA), creatinine (CRE), globuline (GLOB), glucose (GLU), potassium (K^+), sodium (Na^+), phosphate (PHOS), total bilirubin (TBIL), and total protein (TP) was conducted by the UCSD animal care program, diagnostic laboratory services. Each parameter was evaluated by a veterinary pathologist to assess possible nanomaterial-induced toxicity. Statistical evaluation was performed by Student *t* test regarding the mice that received nanoprobes compared to control animals. Group differences resulting in $p < 0.05$ by the Student *t* test were considered statistically significant (*: $p < 0.05$, **: $p < 0.01$, ***: $p < 0.001$).

Tissue sections imaging

Mice perfusion and fixation—Mice were placed in deep anesthesia (2% isoflurane in O_2, 1 L/min) prior to open the chest in a V shape to expose the heart and lungs. Following a cut made into the right atrium, a butterfly needle (25 gauge), connected to a perfusion pump (flow rate: 1.5 mL/min), was inserted into the left ventricle. A saline solution (NaCl, 0.9% w/v, 20 mL) was first injected to flush out the blood followed by injection of a paraformaldehyde solution (PFA, 4% w/v in PBS, 20 mL) to fix the mouse tissues.

Fluorescent labeling of whole animal blood vessels—Lysine-fixable fluorescein isothiocyanate-conjugated dextran (FITC-dextran, 2×10^6 Da, Invitrogen) was used to fluorescently label the bloodstream and locate leaky vessels. Because of its high molecular weight (hydrodynamic radius: 27 nm, as specified by manufacturer), fluorescent dextran can only cross leaky vessels, which results in high and diffuse fluorescence background signal outside the vasculature. FITC-dextran was dissolved in saline (NaCl, 0.9% w/v) to yield a concentration of 0.5 mg/mL. Following PFA fixation (see *Mice perfusion and fixation*), total vasculature was fluorescently labeled by perfusing 2 mL of the prepared solution (flow rate: 0.3 mL/min). Organs (tumors, livers, kidneys, hearts, lungs and brains) were then collected and stored in PFA at 4 °C for 24 h prior to tissue processing for histology.

Histology—After fixation in PFA, organs were transferred in a sucrose solution (30% w/v in H_2O) for at least 24 h at 4 °C. Organs were then frozen in a dry ice/2-methyl butane slurry in presence of optimum cutting temperature (OCT) compound (Tissue-Tek®). The frozen blocks were placed on dry ice for 15-30 min and then stored at -80°C until being processed for frozen sections using a cryostat. Tissues sections (5 μm) were cut and placed on positively charged glass slides. The sections were either mounted with an anti-fading mounting medium containing DAPI (Vectashield® with DAPI) for fluorescent microscopy imaging or stained with hematoxylin and eosin (H&E) and mounted with Cytoseal™ 60 for color camera microscopy imaging. The slides prepared for fluorescence microscopy were stored at 4 °C, whereas H&E slides were stored at room temperature.

Microscopy of histological sections—Fluorescent and color pictures were obtained with a KEYENCE BZ-X700 all-in-one fluorescence microscope (Keyence, Osaka, Japan) equipped with both charge-coupled device (CCD) and color camera. A 80 W metal halide lamp was used as excitation source. DAPI fluorescence was detected with a filter cube composed of a 360 ± 40 nm excitation filter, 400 nm beam splitter, and 460 ± 50 nm emission filter. FITC fluorescence was detected with a filter cube composed of a 470 ± 40 nm excitation filter, 495 nm beam splitter, and 525 ± 50 nm emission filter. IR-780 fluorescence was detected with a filter cube composed of a 747 ± 33 nm excitation filter, 776 nm beam splitter, and 776 nm long-pass emission filter. All acquisitions were performed with a 20× objective PlanApoλ N.A 0.75. High resolution mosaic images were created from multiple images with the BZ-X Analyzer software (Keyence). Tumor necrotic core as well as other organs and tissue structures were analyzed using H&E sections.

3. Results

3.1 Preparation and Characterization of Activatable NIR Fluorescent Nanoprobes

In our nanoprobe design, the responsive polymeric material is of central importance as the speed, sensitivity, and selectivity of signal activation depends on the effectiveness of its interaction with the biological target. Naturally occurring polysaccharides possess a number of appealing characteristics (e.g. biocompatibility, biodegradability, low toxicity, high abundance and low cost) and thus have been increasingly incorporated into a variety of nanoparticle formulations [36]. Because of their high content of functional groups (i.e., hydroxyl, amino or carboxylic acid groups) available for modification, polysaccharides can

be readily transformed and optimized into fast and sensitive responsive carriers [37]. Dextran polymer responsive to acidic pH is obtained in a one-step process by protecting the alcohols on the dextran backbone with acid-labile acetal groups (Figure S1A, *left*) [28]. The acetal functionalization changes the solubility of the polymer from hydrophilic to hydrophobic, thus enabling formulation of acetalated dextran particles encapsulating payload. Particles made from this material disassemble in acidic conditions as the modified polymer returns to its original water-soluble state. A similar solubility switching mechanism to that of the pH-responsive dextran has been applied to the design of a modified dextran responsive to H_2O_2 [27]. In this oxidation-sensitive dextran, H_2O_2-degradable arylboronic esters are used as triggering groups (Figure S1A, *right*).

In our nanoprobes, control of the fluorescence signal is obtained by modulating the formation of non-fluorescent dye aggregates and resulting self-quenching inside particles [38]. High concentrations of NIR-emitting heptamethine cyanine molecules (IR-780, λ_{em} = 790 nm) are encapsulated and randomly distributed in the responsive materials (≥ 10% w/w, see Experimental Section, *Preparation and characterization of polymeric nanoprobes*) to generate reversible short-range interactions between fluorophores, quenching the fluorescence signal ('OFF' state, Figure 2A) and yield a practically non-fluorescent state (Figure 2E *left*, fluorescence imaging). A multitude of possible formulation processes can be used to obtain dye-loaded polymer particles. However, obtaining high loadings (> 10% w/w) is not accessible to every method. To produce polymer capsules encapsulating large amount of IR-780, we favor a single-step electrospray process [39], which consists of applying high voltage to an organic solution containing the responsive polymer and a large number of the imaging agents to break the liquid into a jet of very fine aerosol droplets. As the solvent evaporates in flight, dense, solid polymer particles, with unrivalled payload concentrations, are generated and collected. Dual-responsive NPs (Dual-NPs) were prepared by electrospraying a 50:50 w/w mixture of H_2O_2- and pH-responsive modified dextran (see Experimental Section, *Preparation and characterization of the polymeric nanoprobes*), which led to the formation of particles with a mean diameter of 200 ± 40 nm (Figure S2A, scanning electron micrographs (SEM); Figure S1, ^{1}H NMR). Control nanoprobes include H_2O_2- and pH-only responsive NPs (H_2O_2-NPs, dia.: 150 ± 30 nm, Figure S2B; pH-NPs, dia.: 190 ± 40 nm, Figure S2C), as well as non-responsive poly(lactic-co-glycolic acid) NPs (PLGA, dia.: 140 ± 30 nm, Figure S2D). While keeping the nanoprobes' size below characteristic pore cutoff sizes (i.e., between 380 and 780 nm in diameter for tumors) [40, 41], we favored larger nanoprobes in order to limit half-life in systemic circulation (estimated to be below 30 min), which in turn helps maximizing kinetics of signal activation and ensuring visualization of inflammation in a fast time frame. To prevent aggregation and ensure good in vivo circulation, surface hydrophilization of electrosprayed hydrophobic particles was obtained via incorporation of poloxamer 407, a triblock copolymer composed of hydrophobic polypropylene oxide and hydrophilic polyethylene oxide (PEG), during the electrospray process [42].

Fluorescence activation is obtained upon stimulus-triggered particle disassembly (Figure 1A, schematic) as concentration quenching weakens when dyes are partially released and short-range interactions ceased to dominate (Figure 2E right, fluorescence imaging). Incubation of dual-NPs with increasing concentrations of H_2O_2 (0 – 1 mM) caused a proportional

fluorescence activation that was enhanced under acidic conditions (Figure 2B and Figure S3). When lowering the pH value from 7.4 to 6.0, the detection sensitivity of H_2O_2 increased 3.5-fold (see Experimental Section, *In vitro measurement of fluorescence activation*). The degree of degradation measured by transmission electron microscopy (TEM, Figure 2C) and dynamic light scattering (DLS, Figure 2D) corroborate well with the observed fluorescence activation. At pH 7.4, the morphology (Figure 2C, first row) and the particles count rate (Figure 2D, black squares) remain unchanged, whereas at pH 7.4 + H_2O_2 and pH 6 the integrity of the particles become compromised (Figure 2C, second and third row) and the particles count rate decreases, for example, by 23 ± 1 % (Figure 2D, purple circles) and 48 ± 2 % (Figure 2D, pink triangles) after 6 h of incubation, respectively. When both trigger are present, the level of degradation, which seems to arise from a collective process of bulk and surface erosion (Figure 2C, fourth row), is greatly enhanced as the population of particles is reduced by half after only 30 min of incubation (Figure 2D, blue pentagons). This highlights the synergistic effect that exists between the H_2O_2- and pH-responsive materials composing the dual-NPs, which should translate into greater imaging sensitivity in vivo. In areas of inflammation, activated neutrophils and macrophages can create local extracellular concentrations of H_2O_2 as high as 100 μM [43], which falls within the sensitive range of these NPs. More modest fluorescence activation was obtained with H_2O_2-NPs (Figure S4A). Similarly, pH-NPs showed lower fluorescence activation and inferior stability at physiological pH (Figure S4B). Only dual-NPs' H_2O_2-triggered fluorescence activation was amplified in mildly acidic conditions (Figure S4C) and non-responsive NPs stayed in their 'OFF' state in acidic environment with or without H_2O_2 (Figure S4D).

Nonspecific adsorption of serum proteins is an important aspect that is of great importance as it can reduce colloidal stability and cause the nanoprobes to aggregate, which can in turn hinder their transvascular transport into inflamed tissues and limit their performance [44]. The binding of two model proteins (bovine serum albumin, BSA; ovalbumin, OVA) was evaluated by fluorescence spectroscopy (see Experimental Section, *Quantification of protein adsorption*). Dual-NPs show remarkable resistance in protein adsorption. Compared to the saturated adsorbed protein density values for BSA (290 ng/cm^2) and OVA (313 ng/cm^2) [45], minimal amount of bound proteins were found on the dual-NPs, with 0.33 ± 0.06 ng /cm^2 and 0.45 ± 0.05 ng/cm^2 of BSA and OVA, respectively. The dual-NPs are also stable in total serum as indicated by the negligible change in hydrodynamic diameter and particles count rate measured by DLS (Figure S5A), as well as in spectral signature (maximum emission wavelength), over 24 h incubation at 37°C (Figure S5B). The resistance to non-specific protein adsorption was attributed to the surface PEG layer, which provides a steric barrier, and the nanoprobes' overall neutral charge, which limits the affinity towards abundant negatively charged serum proteins [46].

Because of disparities in intermolecular dye interactions [38], 'OFF' and 'ON' state NPs have different emission maxima (Figure 2F). Silenced NPs, characterized by a high dye loading and, hence, close proximity and strong interactions between dye molecules, present a red-shifted emission maximum centered at 825 nm (Figure 2F, green trace). Activated NPs, characterized by longer intermolecular distances and weaker interactions between dye molecules, possess an emission maximum similar to that of free IR-780 and centered at 790 nm (Figure 2F, red trace). Because of spectral overlap between 'OFF' and 'ON' state

emission and resulting signal crossover, stimulus-triggered fluorescence signal acquired using a single filter set (λ_{ex} = 745 ± 15 nm, λ_{em} = 800 ± 10 nm) consists of a mixture of both 'OFF' and 'ON' state emission; the relative abundance of the two signals depends both on time and concentration of H_2O_2 and H^+ (Figure 2G, yellow signal). The NPs' distinct spectral fingerprints allow quantitative decomposition of the mixed raw signal into its individually resolved fluorescence constituents, i.e., 'OFF' state (Figure 2G, green signal) and 'ON' state signal (Figure 2G, red signal), using multispectral acquisition (emission scanned from 790 to 850 nm) and software-based spectral unmixing algorithms (see Experimental Section, *In vitro measurement of fluorescence activation*). In practical terms, reducing the contribution of the unwanted, detail-obscuring 'OFF' state signal (background) results in a drastic increase in T/B.

3.2 In Vivo Detection of Inflamed Tumor Tissues

The feasibility of using our detection platform to visualize inflammatory microenvironments was first investigated in a mouse 4T1 breast tumor model known to display cancer-associated inflammation (Figure 3, see Experimental Section, *Animal models and in vivo/ex vivo NIR fluorescence imaging*) [47]. Control groups for this study included H_2O_2- and pH-NPs, as well as free IR-780 and indocyanine green (ICG) dyes with 'always ON' fluorescence and non-responsive IR-780-doped PLGA NPs as 'always OFF' NPs. Upon intravenous injection of NPs, a rapid increase in fluorescence intensity was detected at the tumor site (Figure 3A and Figure 3B, arrow 1), which plateaued around 24 h. Dual-NPs demonstrated significantly faster kinetics of activation and stronger fluorescence signal in tumors (Figure 3A). Compared to tissue autofluorescence recorded before injection of the NPs (t = 0 h), dual-NPs presented a 95-fold signal increase in fluorescence in the tumor after 24 h compared to 14 and 45-fold increases for H_2O_2- and pH-NPs, respectively. Tumor-mediated fluorescence activation with dual-NPs (65-fold) is greater than the sum of the signal increase obtained for H_2O_2- and pH-responsive NPs (43-fold), supporting a synergistic effect between the two stimuli-responsive materials. Fluorescence of non-responsive NPs remained relatively unchanged: only 9-fold signal increase due to passive accumulation of particles in tumors. Compared to the widely used nonspecific ICG dye [48], dual-NPs provided enhanced detection sensitivity and an extended imaging window (Figure S6A). Injection of free ICG produced high fluorescence background in the abdominal region and enabled very limited tumor-specific imaging (Figure S6B). At equal dye concentrations, dual-NPs displayed a 161-fold greater fluorescence signal than ICG in the tumor. Furthermore, the fluorescence remained maximum for as long as 96 h, whereas most ICG was cleared from the body by that time. Analysis of whole body fluorescence signal overtime revealed a linear signal clearance and, based on extrapolated data, return to fluorescence basal level should be reached after 14 days (Figure S7).

Unlike the gradual signal increase recorded in the tumor (Figure 3B, arrow 1; Figure 3C, open circles), the background signal contribution peaked in the liver region immediately after NP injection (t = 1 h, Figure 3B, arrow 2; Figure 3C, solid squares) before slowly decreasing thereafter (52% decrease from 1 to 96 h). Using a multispectral acquisition (Figure 3D, left), we can observe two distinct emission profiles. In the tumor area (Figure 3D, left, arrow 1), the emission signal is maximum in the first filter set (λ_{em} = 790-810 nm,

Figure 3E, red squares) and matches the spectral signature of the activated NPs (Figure 2F, red curve), whereas the background signal found in the liver region (Figure 3D, *left*, arrow 2) peaks in the second filter set (λ_{em} = 810-830 nm, Figure 3E, green circles) and is consistent with the spectral signature of the 'silenced' NPs (Figure 2F, green curve). Spectral processing of this multispectral lambda stack acquisition (Figure 3D, *left*) allowed efficient isolation of the individual NPs' emission fingerprints (Figure 3D, right), i.e., 'ON' state signal at the tumor site and 'OFF' state signal in the liver region. Isolated 'ON' state signal in the tumor and other tissues overtime can be found in Figure 3F. The rapid increase of the 'ON' state signal at the tumor site (Figure 3F, open circles) confirmed progressive activation of the NPs in the diseased environment, whereas the weaker 'ON' state signal recorded in the liver region (40-fold slower kinetic, Figure 3F, solid squares) highlighted the NPs' in vivo stability and confirmed that the initial elevated raw background signal in the liver region (Figure 3C, solid squares) resulted from fast accumulation of silenced NPs. Such isolation of the signal of interest ('ON' state signal) is unique to our NP design and rapidly leads to high contrast between inflamed and healthy tissues (Figure 3G and Figure 3H), which alleviates the necessity to wait for substantial activation of the nanoprobes and clearance from normal tissues to achieve good contrast, as it is the case with conventional single channel acquisition (Figure 3G, black squares). Upon spectral unmixing, T/B reached a maximum value of 18.9 ± 0.6 at t = 3 h (Figure 3G, open circles; Figure 3H, 'ON' state fluorescence image and data). At this time, the mixed raw signal from dual-NPs allowed detection of inflamed tumor tissues with a T/B of only 1.15 ± 0.02 (P = 0.038, Figure 3G, solid squares; Figure 3H, raw signal fluorescence image and data). This represents a significant 17fold improvement in T/B (P = 0.0001). Study of the unmixed signals confirmed that background signal in the liver was the result of accumulation of silenced NPs (Figure 3H, green signal), as most of the liver signal can be attributed to 'OFF' state signal (97.3 ± 0.2%, calculated from the signal ratio 'OFF' state signal/total signal). Isolation of activated 'ON' state signal by spectral unmixing reduced background signal by 20 ± 1-fold. For pH- and H_2O_2-responsive NPs, multicolor spectral processing also resulted in significant increases in T/B, but at the cost of reduced activated signal (Figure S8A-F). Due to the absence of significant fluorescence activation, spectrally unmixing imaging data from non-responsive 'always OFF' NPs did not result in improvement of the T/B (Figure S8G-I). Similarly, the imaging performance of 'always ON' free IR-780 dye could not be enhanced by spectral processing, as IR-780 does not present a multispectral signature (Figure S9).

Tumor-specific contrast enhancement was also validated by ex vivo organs (see Experimental Section, *Animal models and in vivo/ex vivo NIR fluorescence imaging*) and tissue sections fluorescence imaging (see Experimental Section, *Tissue sections imaging*). After euthanasia, excised organs were imaged and fluorescence signal was spectrally processed (Figure 4A-B). Before spectral unmixing (raw signal in yellow), the highest fluorescence intensity was found in tumors (not statistically significant) and the major background signal contributor was the liver, which was expected as liver is the primary excretion route for nanoparticles [49]. By suppressing unwanted background signal ('OFF' state in green) using spectral unmixing, the contribution from the liver could be reduced by 40 ± 3% and the tumor contribution increased by 20 ± 2% ('ON' state signal in red). This increases the tumor-to-liver ratio from 1.3 ± 0.1 to 2.7 ± 0.1 (two-fold increase, P = 0.0003).

The major sources of nonspecific activated signals were found in kidneys and lungs (Figure 4B, *red histogram*). Having a large surface constantly in contact with air oxygen, lungs are known to be a site of major ROS production under physiological conditions [50]. Similarly, the medulla of the kidney is considered perpetually hypoxic due to its unique countercurrent capillary network and low blood flow circulation [51]. To investigate if signal activation in those two organs happens naturally or is connected to some extent to nanoprobes activation at the tumor site, we examined organ-specific activity of dual-NPs in tumor-bearing mice versus healthy mice (Figure S10). Interestingly, the results did not show significant differences in nonspecific 'ON' state signal levels between kidneys and lungs harvested from healthy or tumor-bearing mice, which suggests that the NPs' activation in those organs is due to their unique environment. One must note that due to the activatable nature of the nanoprobes, the detected fluorescence intensity is not proportional to the number of nanoprobes present and cannot be used to quantify the biodistribution of the nanoprobes.

A concern presented by nanomaterial uptake in liver and spleen is safety. Therefore, a serum toxicity assay on mice at various time (t = 3, 24, and 96 h) after injection of the NPs was performed to assess potential toxicity of the diagnostic agent (see Experimental Section, *Serum collection and analysis*). As a control, the same volume of PBS 1× (pH 7.4) was injected into another group of mice. A few analytes were increased in NPs treated mice compared to the control group, such as urea and ALT (Figure S11). However, other related chemistries such as creatinine or alkaline phosphatase were not upregulated. Also, for both groups and at all time points, no pathological signs of toxicity were observed, as confirmed with a veterinary pathologist. This suggests that the NPs do not induce acute systemic toxicity in mouse. However, the long-term toxicity needs to be assessed.

To localize the NIR signal from the NPs in the tumor, we performed whole tumor section imaging (Figure 4C-D). Identification of intratumoral structures (e.g. skin, necrotic core, connective tissues) was assessed by hematoxylin and eosin staining (H&E, Figure S12). As seen on the fluorescence microscopic image (transversal section), extensive fluorescence activation could be found in close vicinity to the necrotic core (red signal, Figure 4C and Figure 4D, I), which correlates with malfunctioning vasculature, as revealed by extensive extravasation of FITC-dextran (green signal, Figure 4C, Figure 4D, I). The NIR signal extended throughout the whole tumor with reduced intensity near connective tissues and more functional blood vessels (Figure 4D, II), highlighted by the confined FITC-dextran signal. These observations agrees with previous reports that show how structurally and functionally abnormal tumor vasculature contributes to the inflammatory microenvironment [35]. In contrast to normal vessels, tumor vessels are leaky, tortuous, dilated, excessively branched, and saccular. Consequently, tumor blood flow is chaotic, which leads to impaired blood supply and, hence, hypoxia, acidosis and tissue redox disequilibrium (i.e., promotion of ROS production). Particularly harsh environments are formed beyond the diffusion distance of oxygen from blood vessels (100–150 μm) and adjacent to necrotic cores. NIR fluorescence signal was not detected in the necrotic core (Figure 4D, III) due to its avascular nature, which prevents delivery into that region [52]. Similarly, the skin region in vicinity to the necrotic core was also exempt of fluorescence activation (Figure 4D, IV). The possibility on NIR emission originating from another emission source (i.e., autofluorescence) was ruled

out since no fluorescence signal in the NIR region could be detected in tumors from PBS injected control mice (Figure S13).

3.3 In Vivo Detection of Inflamed Arthritic Joints and Paws

We also evaluated the performance of dual-NPs for detection of inflammation in K/BxN serum-transfer arthritis and carrageenan-induced paw inflammation (see Experimental Section, *Animal models and in vivo/ex vivo NIR fluorescence imaging*, also Figure S14 and S15 for macroscopic appearance of inflamed paws) using the same experimental design as for detection of tumors. Similarly, upon intravenous injection of dual-NPs, increasing inflammation-specific signal was observed in both models, as well as a strong background signal immediately after injection, which increased moderately over the next 7 h (arthritis, Figure 5A and Figure S16A; paw inflammation, Figure 5E and Figure S16B). Isolation of the 'ON' state signal over time using spectral unmixing confirmed that the NPs were progressively activated in regions of inflammation but remained stable in healthy tissues (arthritis, Figure 5B; paw inflammation, Figure 5F). Removal of background signal dramatically increased the target-to-background ratios to reach maximum values of 15 ± 3 (6-fold increase, P = 0.015, Figure 5C and Figure 5D, 'ON' state signal in red) and 22 ± 4 (9-fold increase, $P = 0.0095$, Figure 5G and Figure 5H, 'ON' state signal in red) at 3 h post-injection for arthritic joints and inflamed paw, respectively. Before spectral unmixing, fluorescence was detected at 3 h in arthritic joints and irritant-induced inflamed paws with T/B ratios of 2.5 ± 0.3 ($P = 0.018$, Figure 5D, yellow signal) and 2.5 ± 0.5 ($p = 0.0089$, Figure 5H, yellow signal), respectively. Isolation of activated 'ON' state signal by spectral unmixing reduced background signal contribution by 7 ± 1-fold. Similar to our results in the tumor model, background signal arose mostly from accumulation of non-activated NPs; 'OFF' state signal contributed to most of the signal found in the liver (arthritis: 90 ± 2%, paw inflammation: 92 ± 4%). For both of these inflammation models, spectral unmixing of imaging data using pH- and H_2O_2-responsive NPs showed inflammation-selective fluorescence activation and enhanced T/B, but with lower 'ON' state signal (arthritis: Figure S17A-F, inflamed paw model: Figure S18A-F). Due to the absence of significant fluorescence activation, spectrally unmixing imaging data for non-responsive 'always OFF' NPs did not affect the arthritic joints-to-background (Figure S17G-I) or inflamed paw-to-background signal ratio (Figure S18G-I).

4. Discussion

Combining fast responsive polymeric systems with NIR fluorescent dyes to create robust activatable contrast agents offers a number of advantages. First, these biosensors are highly versatile, as all their constituting elements are interchangeable. A variety of fluorescent dyes and stimuli-responsive polymers can be used to tune NPs' emission and the chemical species to which they selectively respond. As demonstrated in this study, combining materials responsive to complementary biomarkers (e.g. low pH and elevated levels of H_2O_2) during particle formulation allowed detection of inflammatory conditions with greater sensitivity than NPs responsive to only one of these biomarkers. By using a synergistic dual-responsive approach, the probability of triggered activation is increased, thus enhancing overall sensitivity.

In our system, the NPs carry a large fluorescence imaging payload, which can be collectively delivered and activated in disease sites, resulting in large and long-lasting localized signal enhancement. This likely results from our use of lipophilic cationic fluorescent dyes, which exhibit slower clearance kinetics due to their high affinity to dysfunctional mitochondria and other hydrophobic cellular and tissue compartment [53]. Therefore, as the polymeric vehicles disassemble, many released dyes remain in the diseased tissue and the resulting high fluorescence signal persists. The persistence of this imaging signal (days) is also ideal for image-guided surgery [54], for which clinical translation has suffered due to the fast clearance of small hydrophilic dyes (e.g. ICG), limiting the temporal window for surgery to minutes after administration [55].

The large amount of encapsulated dyes stably held in the polymeric nanocarriers is also responsible for the initial ‘silenced’ state (intermolecular quenching). In our case, the main source of background noise results from the NPs' accumulation in blood-filtering organs (e.g. liver, kidneys, and spleen). Even in their ‘silenced’ state, accumulation of non-activated NPs can generate substantial noise, which is especially problematic shortly after injection of NPs when the level of fluorescence activation is not yet high enough to yield good contrast. Because of spectral overlap between ‘OFF’ and ‘ON’ state emissions, conventional single channel fluorescence imaging acquisition results in a T/B (average value of 2.0 ± 0.6 across the three in vivo models of inflammation, t = 3 h) that does not meet the Rose criterion (a T/B of at least 5 is needed to distinguish image features with 100% certainty) [56]. T/B of single channel fluorescence only reached acceptable values at t > 72 h post-injection.

To overcome this obstacle, we show here that spectral unmixing differentiates NPs' distinct emission fingerprints (‘OFF’ state: 825 nm, ‘ON’ state: 790 nm) and enhances the T/B (average value of 19 ± 2 across the three in vivo models of inflammation, t = 3 h) by removing unwanted background signal. Upon spectral unmixing, a facile and rapid process built in the imaging software and executed in a few seconds, T/B met the Rose criterion as early as 1 h after NP injection (9.2 ± 0.7). Emission fingerprinting also provided valuable information on the fate of NPs in vivo. Mapping NPs' ‘ON’ and ‘OFF’ signals provided evidence of NPs' activation in regions of inflammation and stability in healthy tissues. The ability to distinguish signal due to activation versus accumulation could be particularly helpful in reducing the inconveniently elevated incidence of false positives and requirement for invasive biopsy for verification associated with current diagnostic strategies [57, 58].

5. Conclusion

We have developed a system capable of detecting inflammation-associated chemical species with high sensitivity and specificity. Since molecular changes occur before structural, functional, or anatomical changes, our imaging methodology has the potential to facilitate earlier identification of small inflammatory foci and timely clinical intervention. The impact in oncology could be crucial, as early detection greatly enhances survival. Also, high-resolution delineation of primary tumor sites could improve completeness of resection and minimize damage to nearby healthy tissues during surgery. As fluorescence-guided surgery systems (e.g. FluorVivo™, INDEC Biosystems) allow routine real-time multicolor (visible to NIR) image guidance and spectral separation of tissue autofluorescence, we see no

hindrance to clinical translation of our imaging method. Similarly, for autoimmune diseases like arthritis, early treatment can halt disease progression and prevent irreversible disability. [59] Furthermore, in biomedical research, our platform could replace common invasive techniques (e.g. histology) that require sacrificing animals by providing real-time, non-invasive imaging of inflammation.

As the field of stimuli-responsive polymers is constantly growing and more indicative biomarkers of physiological and pathological processes are discovered, new design principles may be employed in similar activatable imaging strategies. Although stimuli-responsive polymer-based detection systems are still in their infancy compared to their small molecule analogues, they have the potential to bridge the gap between the tremendous promise of activatable imaging probes (monitoring of metabolic reactions and sensitive, precise detection of disease) and their clinical application.

Supplementary Material

Refer to Web version on PubMed Central for supplementary material.

Acknowledgments

This research was made possible by an NIH New Innovator Award (DP 2OD006499), King Abdulaziz City for Science and Technology (through the KACST-UCSD Center of Excellence in Nanomedicine and Engineering), National Institutes of Arthritis and Musculoskeletal and Skin (MG: 1K08AR064834), NCRR (S10 RR027970), and NIH/NHLBI (P01 HL091830). NMR data was acquired at the UCSD Skaggs School of Pharmacy and Pharmaceutical Sciences NMR Facility. Serum biochemistry was undertaken and analyzed by the UCSD Animal Care Program Diagnostic Services Laboratory. Histological services were performed by the Moores Cancer Center Histology Core. Fluorescence imaging of the histological sections were performed at the UCSD School of Medicine Microscopy Core (NCI Support Grant P30 2P30CA023100-28). Animal imaging was done at the UCSD Animal Care Program Phenotyping Core. Usage of the IVIS® Spectrum permitted by Ellen C. Breen. The authors would like to express their gratitude to Arnold Garcia for his help with the animal experiments, to Minnie Chan and Sophia Suarez for their help with ^{1}H NMR, to Ken Osborne for his help with interpretation of the serum biochemistry data, to Nissi Varki for her help with histopathology analysis and to Beatrix Bartok for her valuable input.

References

1. Weissleder R, Ntziachristos V. Shedding light onto live molecular targets. Nat Med. 2003; 9:123–8. [PubMed: 12514725]
2. Massoud TF, Gambhir SS. Molecular imaging in living subjects: seeing fundamental biological processes in a new light. Gene Dev. 2003; 17:545–80. [PubMed: 12629038]
3. Etzioni R, Urban N, Ramsey S, McIntosh M, Schwartz S, Reid B, et al. The case for early detection. Nat Rev Cancer. 2003; 3:243–52. [PubMed: 12671663]
4. Hellebust A, Richards-Kortum R. Advances in molecular imaging: targeted optical contrast agents for cancer diagnostics. Nanomedicine. 2012; 7:429–45. [PubMed: 22385200]
5. Frangioni JV. New technologies for human cancer imaging. J Clin Oncol. 2008; 26:4012–21. [PubMed: 18711192]
6. Lei JP, Ju HX. Signal amplification using functional nanomaterials for biosensing. Chem Soc Rev. 2012; 41:2122–34. [PubMed: 22278386]
7. Xu JJ, Zhao WW, Song SP, Fan CH, Chen HY. Functional nanoprobes for ultrasensitive detection of biomolecules: an update. Chem Soc Rev. 2014; 43:1601–11. [PubMed: 24342982]
8. Longmire M, Choyke PL, Kobayashi H. Clearance properties of nano-sized particles and molecules as imaging agents: considerations and caveats. Nanomedicine. 2008; 3:703–17. [PubMed: 18817471]

9. Chang J, Graber HL, Barbour RL. Improved reconstruction algorithm for luminescence optical tomography when background lumiphore is present. Appl Optics. 1998; 37:3547–52.
10. Weinberger AWA, Lappas A, Mazinani BAE, Huth J, Mohammadi B, Walter P. Pre-injection fluorescence in indocyanine green (ICG) angiography: Pseudofluorescence and autofluorescence. Invest Ophth Vis Sci. 2005; 46
11. Kobayashi H, Choyke PL. Target-Cancer-Cell-Specific Activatable Fluorescence Imaging Probes: Rational Design and in Vivo Applications. Accounts Chem Res. 2011; 44:83–90.
12. Luby BM, Charron DM, MacLaughlin CM, Zheng G. Activatable fluorescence: From small molecule to nanoparticle. Adv Drug Deliv Rev. 2016 ahead of print.
13. Hsu BY, Ng M, Tan A, Connell J, Roberts T, Lythgoe M, et al. pH-Activatable MnO-Based Fluorescence and Magnetic Resonance Bimodal Nanoprobe for Cancer Imaging. Adv Healthc Mater. 2016; 5:721–9. [PubMed: 26895111]
14. Ruiz-Gonzalez R, Bresoli-Obach R, Gulias O, Agut M, Savoie H, Boyle RW, et al. NanoSOSG: a Nanostructured Fluorescent Probe for the Detection of Intracellular Singlet Oxygen. Angew Chem. 2017; 56:1–5.
15. Wang L, Zhu X, Xie C, Ding N, Weng XF, Lu WY, et al. Imaging acidosis in tumors using a pH-activated near-infrared fluorescence probe. Chem Commun. 2012; 48:11677–9.
16. Wang YG, Zhou KJ, Huang G, Hensley C, Huang XN, Ma XP, et al. A nanoparticle-based strategy for the imaging of a broad range of tumours by nonlinear amplification of microenvironment signals. Nat Mater. 2014; 13:204–12. [PubMed: 24317187]
17. Kundu K, Knight SF, Willett N, Lee S, Taylor WR, Murthy N. Hydrocyanines: A Class of Fluorescent Sensors That Can Image Reactive Oxygen Species in Cell Culture, Tissue, and In Vivo. Angew Chem. 2009; 48:299–303. [PubMed: 19065548]
18. Wang Y, Wang C, Li Y, Huang G, Zhao T, Ma X, et al. Digitization of Endocytic pH by Hybrid Ultra-pH-Sensitive Nanoprobes at Single-Organelle Resolution. Adv Mater. 2017; 29:1603794.
19. Oh WK, Jeong YS, Kim S, Jang J. Fluorescent polymer nanoparticle for selective sensing of intracellular hydrogen peroxide. Acs Nano. 2012; 6:8516–24. [PubMed: 22971112]
20. Myochin T, Kiyose K, Hanaoka K, Kojima H, Terai T, Nagano T. Rational design of ratiometric near-infrared fluorescent pH probes with various pKa values, based on aminocyanine. J Am Chem Soc. 2011; 133:3401–9. [PubMed: 21341656]
21. Song D, Cho S, Han Y, You Y, Nam W. Ratiometric fluorescent probes for detection of intracellular singlet oxygen. Org Lett. 2013; 15:3582–5. [PubMed: 23808624]
22. Kim M, Seo YH, Kim Y, Heo J, Jang WD, Sim SJ, et al. A fluorogenic molecular nanoprobe with an engineered internal environment for sensitive and selective detection of biological hydrogen sulfide. Chem Commun. 2017; 53:2275–8.
23. Valdes PA, Leblond F, Jacobs VL, Wilson BC, Paulsen KD, Roberts DW. Quantitative, spectrally-resolved intraoperative fluorescence imaging. Sci Rep. 2012; 2:798. [PubMed: 23152935]
24. Vereb G, Jares-Erijman E, Selvin PR, Jovin TM. Temporally and spectrally resolved imaging microscopy of lanthanide chelates. Biophys J. 1998; 74:2210–22. [PubMed: 9591648]
25. Feng X, Zhang T, Liu JT, Miao JY, Zhao BX. A new ratiometric fluorescent probe for rapid, sensitive and selective detection of endogenous hydrogen sulfide in mitochondria. Chem Commun. 2016; 52:3131–4.
26. Hou Y, Zhou J, Gao Z, Sun X, Liu C, Shangguan D, et al. Protease-activated ratiometric fluorescent probe for pH mapping of malignant tumors. Acs Nano. 2015; 9:3199–205. [PubMed: 25670342]
27. Broaders KE, Grandhe S, Frechet JM. A biocompatible oxidation-triggered carrier polymer with potential in therapeutics. J Am Chem Soc. 2011; 133:756–8. [PubMed: 21171594]
28. Bachelder EM, Beaudette TT, Broaders KE, Dashe J, Frechet JMJ. Acetal-derivatized dextran: An acid-responsive biodegradable material for therapeutic applications. J Am Chem Soc. 2008; 130:10494–5. [PubMed: 18630909]
29. Gatenby RA, Gillies RJ. Why do cancers have high aerobic glycolysis? Nat Rev Cancer. 2004; 4:891–9. [PubMed: 15516961]
30. Winterbourn CC. Reconciling the chemistry and biology of reactive oxygen species. Nat Chem Biol. 2008; 4:278–86. [PubMed: 18421291]

31. Kellum JA, Song MC, Li JY. Science review: Extracellular acidosis and the immune response: clinical and physiologic implications. Crit Care. 2004; 8:331–6. [PubMed: 15469594]
32. Chiche J, Brahimi-Horn MC, Pouyssegur J. Tumour hypoxia induces a metabolic shift causing acidosis: a common feature in cancer. J Cell Mol Med. 2010; 14:771–94. [PubMed: 20015196]
33. Yuan F, Dellian M, Fukumura D, Leunig M, Berk DA, Torchilin VP, et al. Vascular-Permeability in a Human Tumor Xenograft - Molecular-Size Dependence and Cutoff Size. Cancer Res. 1995; 55:3752–6. [PubMed: 7641188]
34. Haywood L, Walsh DA. Vasculature of the normal and arthritic synovial joint. Histol Histopathol. 2001; 16:277–84. [PubMed: 11193203]
35. Carmeliet P, Jain RK. Angiogenesis in cancer and other diseases. Nature. 2000; 407:249–57. [PubMed: 11001068]
36. Saravanakumar G, Jo DG, Park JH. Polysaccharide-Based Nanoparticles: A Versatile Platform for Drug Delivery and Biomedical Imaging. Curr Med Chem. 2012; 19:3212–29. [PubMed: 22612705]
37. Wen Y, Oh JK. Recent Strategies to Develop Polysaccharide-Based Nanomaterials for Biomedical Applications. Macromol Rapid Commun. 2014; 35:1819–32. [PubMed: 25283788]
38. Viger ML, Live LS, Therrien OD, Boudreau D. Reduction of self-quenching in fluorescent silica-coated silver nanoparticles. Plasmonics. 2008; 3:33–40.
39. Almeria B, Deng WW, Fahmy TM, Gomez A. Controlling the morphology of electrospray-generated PLGA microparticles for drug delivery. J Colloid Interf Sci. 2010; 343:125–33.
40. Hobbs SK, Monsky WL, Yuan F, Roberts WG, Griffith L, Torchilin VP, et al. Regulation of transport pathways in tumor vessels: role of tumor type and microenvironment. PNAS. 1998; 95:4607–12. [PubMed: 9539785]
41. Hashizume H, B P, Morikawa S, McLean JW, Thurston G, Roberge S, Jain RK, McDonald DM. Openings between defective endothelial cells explain tumor vessel leakiness. Am J Pathol. 2000; 156:1363–80. [PubMed: 10751361]
42. Seth A, Katti DS. A one-step electrospray-based technique for modulating morphology and surface properties of poly(lactide-co-glycolide) microparticles using Pluronics (R). Int J Nanomed. 2012; 7:5129–36.
43. Schröder, E., Eaton, P. Redox Signaling and Regulation in Biology and Medicine. Weinheim, Germany: Wiley-VCH Verlag GmbH & Co. KGaA; 2009. Hydrogen Peroxide and Cysteine Protein Signaling Pathways.
44. McKeon KD, L BJ. The presence of adsorbed proteins on particles increases aggregated particle sedimentation, as measured by a light scattering technique. J Adhes. 2008; 84:664–74.
45. Cantarero LA, Butler JE, Osborne JW. The Adsorptive Characteristics of Proteins for Polystyrene and Their Significance in Solid-Phase Immunoassays. Anal Biochem. 1980; 105:375–82. [PubMed: 7006446]
46. Blanco E, Shen H, Ferrari M. Principles of nanoparticle design for overcoming biological barriers to drug delivery. Nature Biotechnol. 2015; 33:941–51. [PubMed: 26348965]
47. Liao D, Luo YP, Markowitz D, Xiang R, Reisfeld RA. Cancer Associated Fibroblasts Promote Tumor Growth and Metastasis by Modulating the Tumor Immune Microenvironment in a 4T1 Murine Breast Cancer Model. Plos One. 2009; 4:e7965. [PubMed: 19956757]
48. Hillman EMC, Amoozegar CB, Wang T, McCaslin AFH, Bouchard MB, Mansfield J, et al. In vivo optical imaging and dynamic contrast methods for biomedical research. Philos T R Soc A. 2011; 369:4620–43.
49. Cho MJ, Cho WS, Choi M, Kim SJ, Han BS, Kim SH, et al. The impact of size on tissue distribution and elimination by single intravenous injection of silica nanoparticles. Toxicol Lett. 2009; 189:177–83. [PubMed: 19397964]
50. Tkaczyk J, Vizek M. Oxidative stress in the lung tissue--sources of reactive oxygen species and antioxidant defence. Prague medical report. 2007; 108:105–14.
51. Manotham K, Tanaka T, Ohse T, Kojima I, Miyata T, Inagi R, et al. A biologic role of HIF-1 in the renal medulla. Kidney Int. 2005; 67:1428–39. [PubMed: 15780095]
52. Jain RK. Delivery of molecular and cellular medicine to solid tumors. Adv Drug Deliver Rev. 2001; 46:149–68.

53. Zhang C, Liu T, Su YP, Luo SL, Zhu Y, Tan X, et al. A near-infrared fluorescent heptamethine indocyanine dye with preferential tumor accumulation for in vivo imaging. Biomaterials. 2010; 31:6612–7. [PubMed: 20542559]

54. Gioux S, Choi HS, Frangioni JV. Image-Guided Surgery Using Invisible Near-Infrared Light: Fundamentals of Clinical Translation. Mol Imaging. 2010; 9:237–55. [PubMed: 20868625]

55. Merian J, Gravier J, Navarro F, Texier I. Fluorescent Nanoprobes Dedicated to in Vivo Imaging: From Preclinical Validations to Clinical Translation. Molecules. 2012; 17:5564–91. [PubMed: 22576228]

56. Bushberg, JT., Seibert, A., Leidholdt, EM., Boone, JM. The essential physics of medical imaging. 2nd. Philadelphia, USA: Lippincott Williams and Wilkins; 2002.

57. Berg WA, Zhang Z, Lehrer D, Jong RA, Pisano ED, Barr RG, et al. Detection of Breast Cancer With Addition of Annual Screening Ultrasound or a Single Screening MRI to Mammography in Women With Elevated Breast Cancer Risk. Jama. 2012; 307:1394–404. [PubMed: 22474203]

58. Long NM, Smith CS. Causes and imaging features of false positives and false negatives on F-PET/CT in oncologic imaging. Insights Imaging. 2011; 2:679–98. [PubMed: 22347986]

59. Ospelt C, Brentano F, Rengel Y, Stanczyk J, Kolling C, Tak PP, et al. Overexpression of Toll-like Receptors 3 and 4 in Synovial Tissue From Patients With Early Rheumatoid Arthritis: Toll-like Receptor Expression in Early and Longstanding Arthritis. Arthritis Rheum. 2008; 58:3684–92. [PubMed: 19035519]

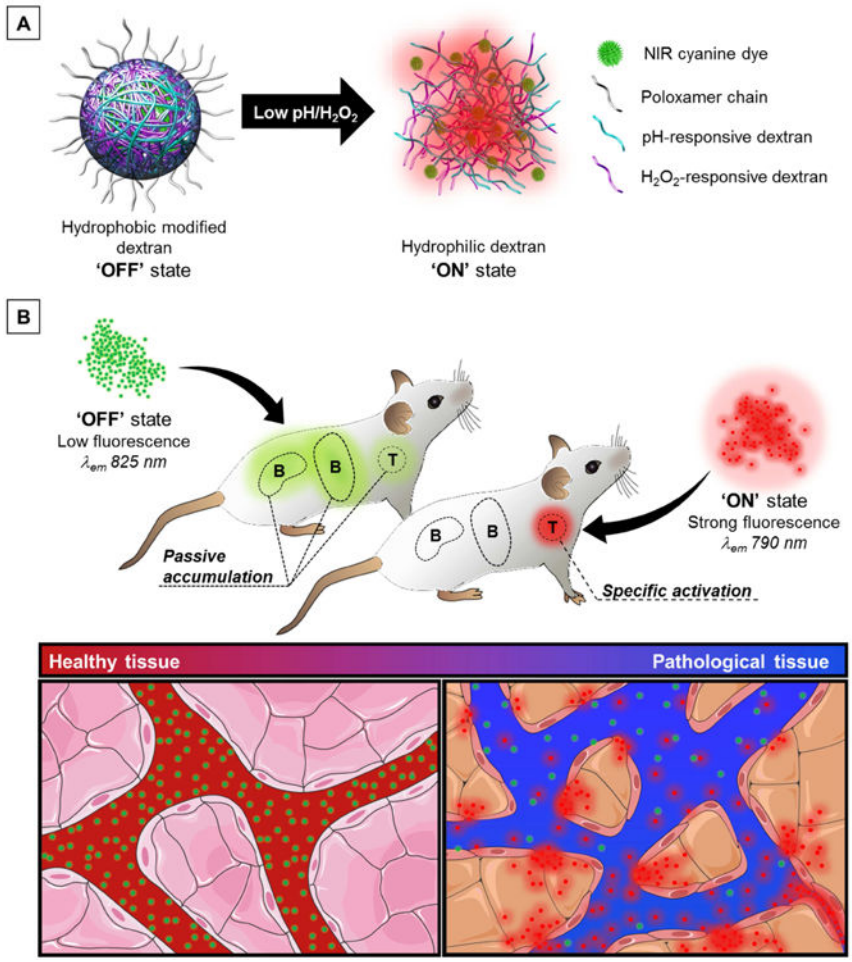

Figure 1. Schematic representation: imaging of inflamed environments using the dual-responsive nanoprobes

(A) pH- and H_2O_2-responsive polymeric materials control the fluorescent intensity and spectral profile of many NIR lipophilic cationic IR-780 dye molecules. Particles disassemble under acidic and/or oxidative stress conditions as the modified polymers return to their native water-soluble state, which release large amount of dyes, relieves self-quenching and triggers fluorescence activation. (B) The nanoprobes remain in their 'OFF' state during blood circulation and in healthy tissues. After reaching pathological tissues, the nanoprobes are turned 'ON' by extracellular acidosis and oxidative stress. The nanoprobes possess distinct emission fingerprints ('OFF' state: 825 nm, 'ON' state: 790 nm), which can be isolated using a spectral unmixing methodology. This enables removal of unwanted background signal (passive accumulation) and detection of inflamed tissues with high target-to-background ratio (T/B) within a few hours. Adapted from Servier Medical Art.

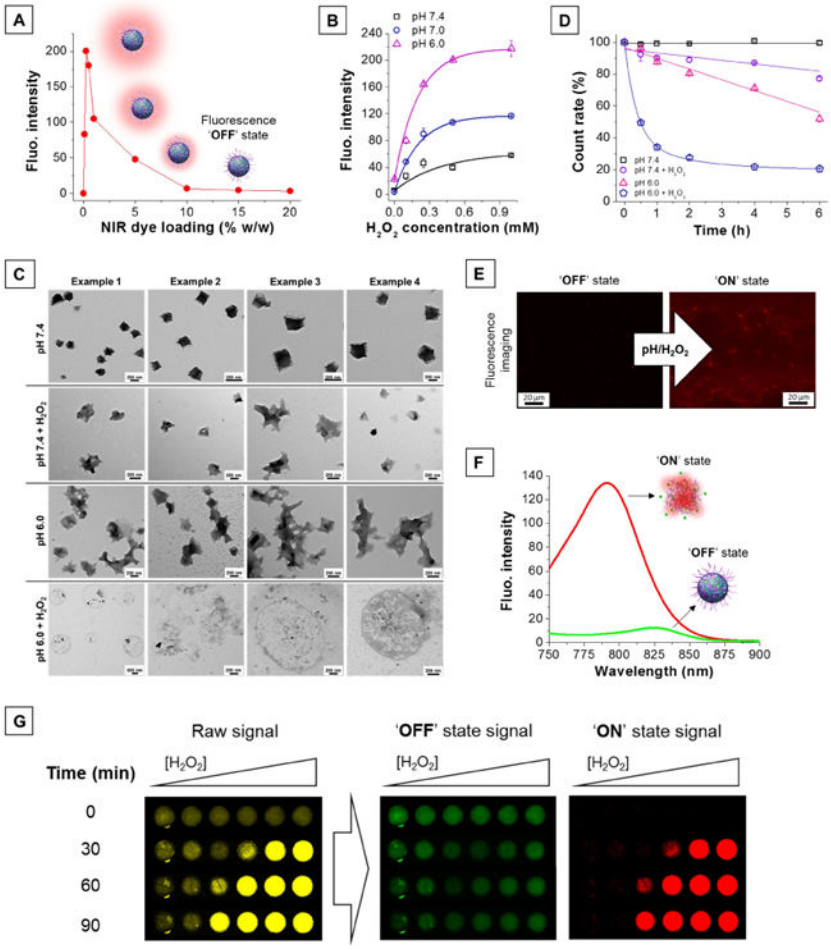

Figure 2. Characterization of pH/H_2O_2-activatable NIR fluorescent nanoprobes

(A) High dye loading in nanoprobes results in quenching of their fluorescence properties, creating an 'OFF' state. (B) H_2O_2-triggered fluorescence activation of dual-responsive nanoprobes is enhanced at low pH. (C) Transmission electron micrographs of the nanoprobes in different environments (pH 7.4, pH 7.4 + H_2O_2, pH 6.0, pH 6.0 + H_2O_2). [H_2O_2] = 0.25 mM, T = 37°C, incubation time: 2 h. (D) Number of nanoprobes over time in different environments (pH 7.4, pH 7.4 + H_2O_2, pH 6.0, pH 6.0 + H_2O_2) represented as percent of initial DLS count rate. [H_2O_2] = 0.25 mM, T = 37°C. (E) Fluorescence microscopic images of the nanoprobes before (left) and after (right) activation. [H_2O_2] = 0.25 mM, pH = 6, incubation time: 1 h. (F) Silenced ('OFF' state, green trace) and activated ('ON' state, red trace) nanoprobes possess different emission maxima. (G) H_2O_2-triggered (0 - 1 mM) fluorescence signal acquired using a single filter set (λ_{ex} = 745 ± 15 nm, λ_{em} = 800 ± 10 nm) consists of a mixture of both 'OFF' and 'ON' state emission (raw signal, yellow). The NPs' distinct spectral fingerprints allow quantitative decomposition of the mixed raw signal into its individually resolved fluorescence constituents, i.e., 'OFF' state (green) and 'ON' state signal (red), using multispectral acquisition (λ_{ex} = 745 ± 15 nm, emission scanned from 790 to 850 nm) and software-based spectral unmixing algorithms. Higher concentrations of H_2O_2 yield faster and greater fluorescence activation.

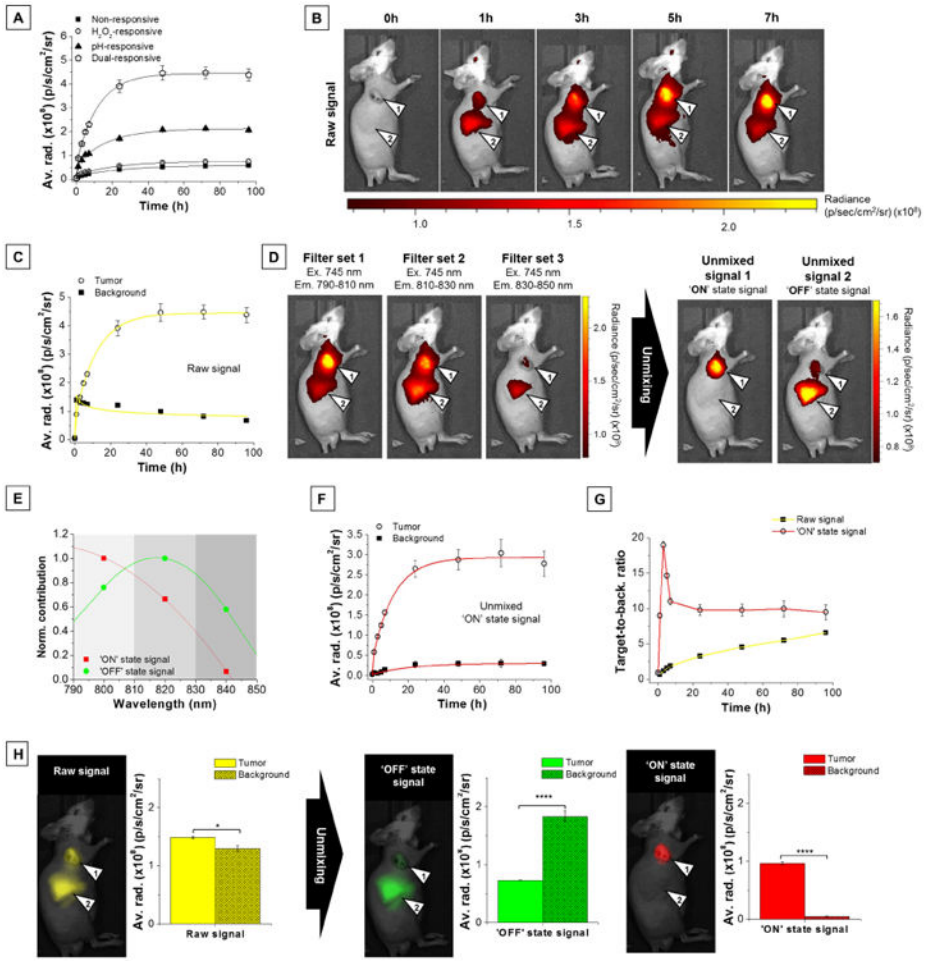

Figure 3. Isolation of activated signal by spectral unmixing increases specificity of detection of inflamed tumor tissues

(A) Raw NIR fluorescence intensity (average radiance) in the tumor as a function of time (0 – 96 h) after injection of various nanoprobes (4 mg/kg). (B) Representative raw fluorescence images (single filter acquisition, λ_{ex} = 745 ± 15 nm, λ_{em} = 800 ± 10 nm) of a tumor-bearing mouse (arrow 1: tumor, arrow 2: background). (C) Raw signal fluorescence data (average radiance) for tumor (open circles) and background (solid squares) at various times after injection of dual-responsive NPs (4 mg/kg). (D) Representative multispectral lambda stack acquisition using selected IR-780-specific filters and resulting fluorescence images of the two unmixed components obtained after spectral unmixing process. Tumors and liver background are indicated by arrow 1 and 2, respectively. (E) Two-components unmixing spectral data obtained using Living Image 4.3.1 software. (F) Unmixed 'ON' state fluorescence data for tumor (open red circles) and background (solid red squares) at various times after injection of dual-responsive NPs. (G) Raw (solid yellow squares) and 'ON' state (open red circles) fluorescence intensity ratio between tumor and background (T/B) as a function of time after injection of dual-responsive NPs. (H) Representative fluorescence images of a tumor-bearing mouse and corresponding raw and unmixed fluorescence data for tumor and background 3 h after injection of dual-responsive NPs. Raw, 'OFF' state, and 'ON' state fluorescence emission pseudocolored in yellow, green, and red, respectively.

Tumors and liver background are indicated by arrow 1 and 2, respectively. Data are presented as mean ± s.e.m. (n = 5 per group). *P ≤ 0.05, ****P ≤ 0.0001

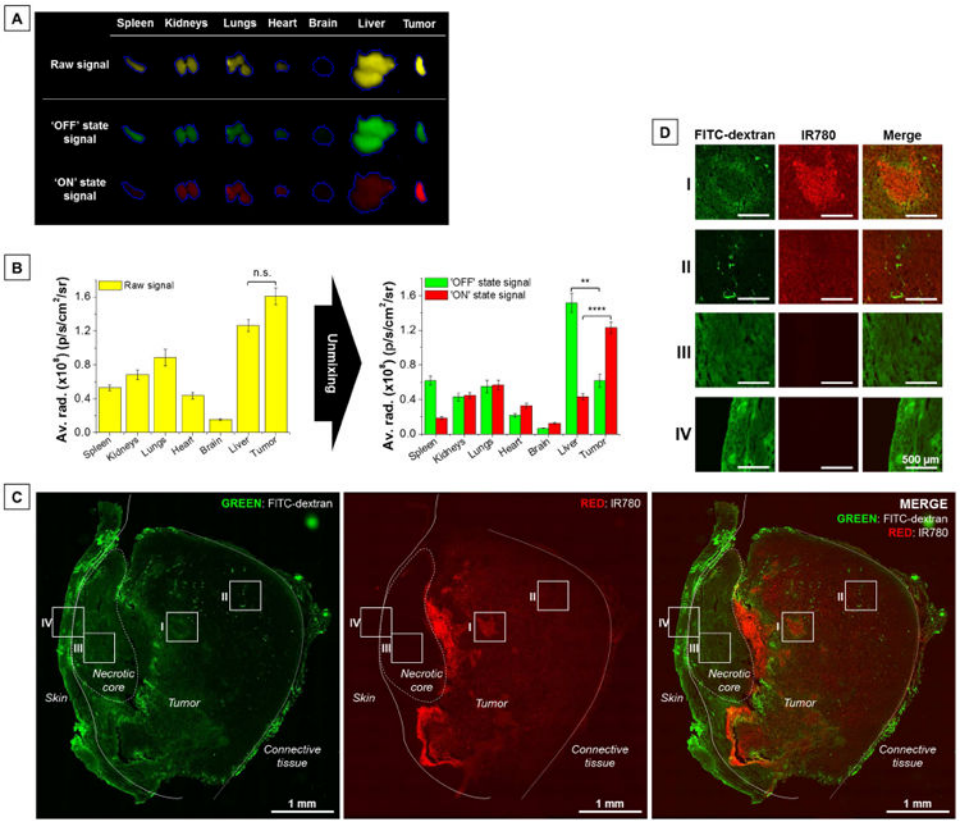

Figure 4. Ex vivo organs and tissue sections imaging

(A) Representative fluorescence images of ex vivo tumors and major organs before (raw signal) and after unmixing (‘OFF’ state signal; ‘ON’ state signal) 7 h post-injection. (B) Fluorescence signal distribution in organs before (raw signal) and after unmixing (‘OFF’ state signal; ‘ON’ state signal) 7 h post-injection. Fluorescence imaging of a (C) representative tumor transversal section and (D) magnified field of views (I: leaky and chaotic blood vessels, harsh environment; II: more functional tumor blood vessels; III: tumor necrotic core; IV: mouse skin). Green: fluorescence signal from FITC-dextran (visualization of tumor vasculature). Red: fluorescence signal of the IR-780 dye from the nanoprobes. No background correction. Data are presented as mean ± s.e.m. (n = 5 per group). n.s. $P > 0.05$, **$P \leq 0.01$, ****$P \leq 0.0001$.

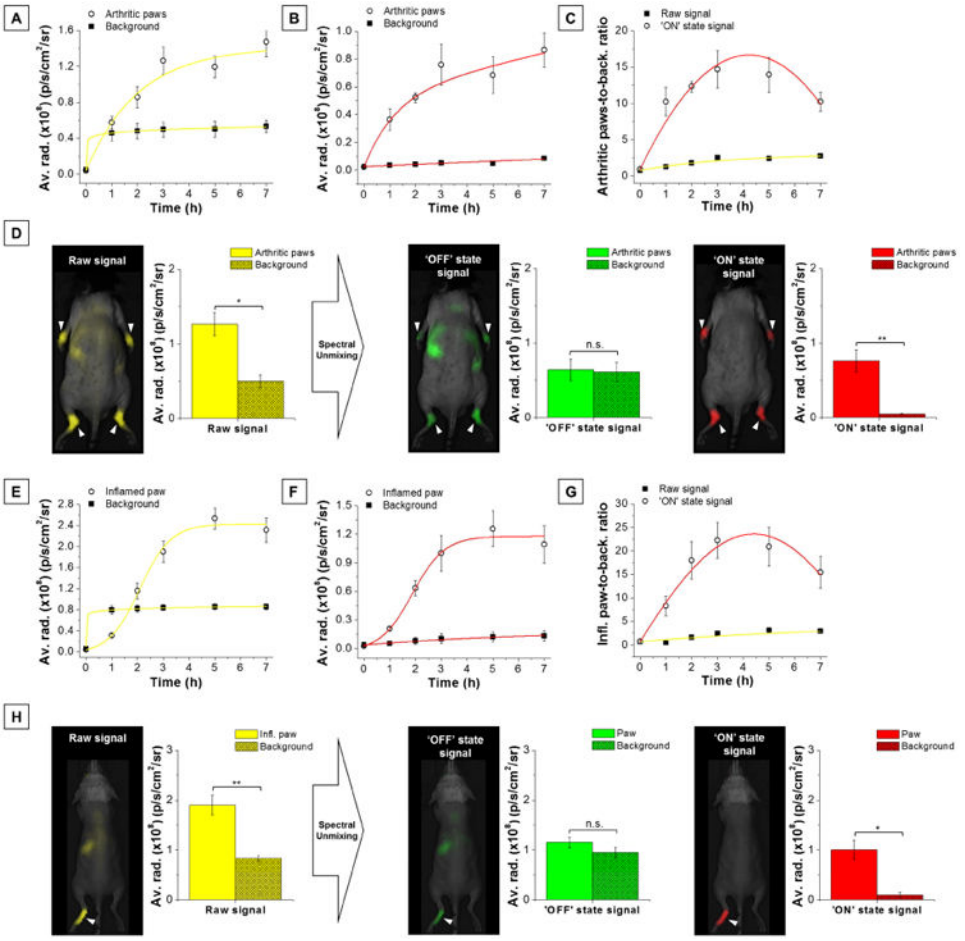

Figure 5. Spectrally-resolved imaging leads to detection of inflammatory microenvironments with greater specificity

Raw fluorescence data (average radiance) for (A) arthritic joints or (E) inflamed paw and background at various times after injection of dual-responsive NPs (4 mg/kg). Inflamed regions, open yellow circles; background, solid yellow squares. Unmixed 'ON' state fluorescence data for (B) arthritic joints or (F) inflamed paw and background at various times after injection of dual-responsive NPs. Inflamed regions, open red circles; background, solid red squares. Raw (yellow line, solid squares) and 'ON' state (red line, open circles) fluorescence intensity ratio between (C) arthritic joints or (G) inflamed paw and background (T/B) as a function of time after injection of dual-responsive NPs. (D-H) Representative fluorescence image of a mouse with (D) K/BxN serum-induced arthritis or (H) carrageenan-induced paw inflammation and corresponding fluorescence data before (raw signal in yellow) and after spectral unmixing ('OFF' state signal in green, 'ON' state signal in red) in inflamed regions and the rest of the body (background) 3 h post-injection of dual-responsive NPs. Data are presented as mean ± s.e.m. (n = 4 mice per group for arthritis and n = 5 mice per group for paw inflammation). Clinical arthritis joint score: 3.4 ± 0.1. Background signal major contributors: spleen and liver. n.s. $P > 0.05$, *$P \leq 0.05$, **$P \leq 0.01$